



# The Prospect of $Y_2SiO_5$ -Based Materials as Protective Layer in Environmental Barrier Coatings

E. García, P. Miranzo, and M.I. Osendi

(Submitted October 16, 2012; in revised form February 13, 2013)

**Bulk yttrium monosilicate ( $Y_2SiO_5$ ) possesses interesting properties, such as low thermal expansion coefficient and stability in water vapor atmospheres, which make it a promising protective layer for SiC-based composites, intended for the hottest parts in the future gas turbines. Because protective layers are commonly applied by thermal spraying techniques, it is important to analyze the changes in structure and properties that these methods may produce in yttrium silicate coatings. In this work, two  $SiO_2$ - $Y_2O_3$  compositions were flame sprayed in the form of coatings and beads. In parallel, the beads were spark plasma sintered at relatively low temperature to obtain partially amorphous bulk specimens that are used as model bulk material. The thermal aging—air and water vapor atmosphere—caused extensive nucleation of  $Y_2SiO_5$  and  $Y_2Si_2O_7$  in both the bulk and coating. The rich water vapor condition caused the selective volatilization of  $SiO_2$  from  $Y_2Si_2O_7$  at the specimen surface leaving a very characteristic micro-ridged  $Y_2SiO_5$  zones—either in coatings or sintered bodies. An important increase in the thermal conductivity of the aged materials was measured. The results of this work may be used as a reference body for the production of  $Y_2SiO_5$  coatings using thermal spraying techniques.**

**Keywords** beads, crystallization, environmental barrier coatings, thermal conductivity, water vapor corrosion, yttrium silicate

## 1. Introduction

The forthcoming substitution of Ni-based superalloys by Si-based ceramic matrix composites (CMCs), carbon-fiber-reinforced SiC (C/SiC) or SiC/SiC, in the structural hot-section parts of gas turbine components will increase the efficiency of these energy production and propulsion systems. These systems may work at higher temperatures, thus reducing the specific fuel consumption and the emission of harmful combustion products (Ref 1, 2). The lower density of ceramic-based components decreases the weight of rotating components and increases the thrust-to-weight ratio for air turbines (Ref 2). A challenge that these ceramic composites must face is the oxidation in oxygen rich atmospheres at high temperature and their corrosion in combustion environments—water vapor rich—that produces problems of recession in the SiC-based CMCs, caused by loss of the  $SiO_2$  layer that protects these systems against further oxidation (Ref 3-6).

Different coating materials have been explored to hinder the hazardous effects of combustion environments.

The characteristics required to the candidate material are, on one side, their mechanical and chemical compatibility with the substrate and, on the other, their performance against combustion gases; i.e., material should have a high chemical stability, low evaporation rate, and low oxygen permeation. Among the different compositions that have been surveyed, rare earth monosilicates stand out as one of the best options for the top layer coating in multilayered systems (Ref 7, 8).

Since Ogura et al. (Ref 8) proposed  $Y_2SiO_5$  as an oxidation barrier, different studies have been devoted to the synthesis of stoichiometric  $Y_2SiO_5$  powders (Ref 9) and bulks (Ref 10), in order to precisely determine its thermal and mechanical properties (Ref 11, 12). Some studies have explored different methods to deposit coatings of this composition, as for instance dip coating (Ref 13), electrophoretic deposition (Ref 14), or paintbrushing of pastes (Ref 15). All these methods require a thermal treatment at high temperature to achieve dense coatings for low oxygen permeation. Conversely, thermal spraying is a quite direct method for coating deposition that imparts high temperatures to the feedstock particles, and henceforth produces certain amorphization and selective volatilization—typically of  $SiO_2$  for silicate-based materials—during projection (Ref 16, 17). Therefore, formation of new phases that may be more easily corroded by the combustion atmospheres could happen. Surprisingly, this shift in the composition and the possible way to avoid it has not been addressed before in thermally sprayed yttrium silicate coatings (Ref 18, 19).

Although the functionality of  $Y_2SiO_5$  coatings as barrier against oxidation has been tested in several works, using

E. García, P. Miranzo, and M.I. Osendi, Institute of Ceramics and Glass, ICV—CSIC, Kelsen 5, 28049 Madrid, Spain. Contact e-mail: garcia@icv.csic.es.

O<sub>2</sub> rich and combustion simulated environments (Ref 7, 8, 15, 18, 19), it has not been studied in detail how these environments modify the microstructure of the coatings. Moreover, the evolution of phases caused by the unbalanced Y<sub>2</sub>SiO<sub>5</sub> composition of the as-sprayed coatings and its effect on key properties of coatings like the hardness and thermal conductivity, determinant for evaluating the full potential of these coatings, have not been addressed at all.

The measurement of the thermal conductivity in coatings by the laser-flash method has the shortcoming of getting freestanding specimens of the precise dimensions required by this test (Ref 20). An alternative procedure could be the employ of similar bulk specimens, as we show in this work, prepared by spark plasma sintering (SPS) flame-sprayed beads of same composition as the coatings. Due to the rapid sintering rates typical of SPS, these materials are expected to retain the microstructure and phases of the flame-sprayed beads (Ref 21), and therefore, may be a convenient model for coatings.

In this work, flame-sprayed coatings and SPS bulk specimens are processed from a feedstock modified to reproduce Y<sub>2</sub>SiO<sub>5</sub> composition after flame spraying, thus accounting for shift in the original Y<sub>2</sub>SiO<sub>5</sub> composition caused by flame spraying. These samples, subjected to air and water vapor thermal aging tests, were studied looking for changes in the microstructure, phases, and properties (hardness and thermal conductivity), and compared to the as-sprayed coatings and SPS materials.

## 2. Experimental

### 2.1 Powder Processing

High purity (>99.7%) powders of SiO<sub>2</sub> (Strem Chemical, France), and Y<sub>2</sub>O<sub>3</sub> (H.C. Starck, Germany), with a mean particle size of 114 and 1 μm, respectively, were used as raw materials. Two compositions (henceforth expressed in mole fraction): C1 (0.5 SiO<sub>2</sub>:0.5 Y<sub>2</sub>O<sub>3</sub>) and C2 (0.57 SiO<sub>2</sub>:0.43 Y<sub>2</sub>O<sub>3</sub>), the last silica enriched respecting the Y<sub>2</sub>SiO<sub>5</sub> composition, were prepared. Location of both compositions in the Y<sub>2</sub>O<sub>3</sub>-SiO<sub>2</sub> equilibrium phase diagram (Ref 22) is shown in Fig. 1. They were prepared by mixing the powders in water in the proportion of 50 wt.% of solid content, adding also 0.4 wt.% of a polyelectrolyte dispersant (Dolapix CE 64 CA, Zschimmer-Schwarz, Lahnstein, Germany) and 5 wt.% of a polysaccharide binder (KB 1247, Zschimmer-Schwarz, Lahnstein, Germany) to stabilize the suspensions and confer enough consistency to the granules after the spray drying process. A blade mixer and an attrition mill were used for the thoroughly mixing of all ingredients and to effectively reduce the particle size of silica powders. No contamination attributable to the milling media (ZrO<sub>2</sub> balls of 2 mm diameter) was detected in the powders according to results of X-ray fluorescence (XRF) analysis (MagiX Pro, Philips, the Netherlands) performed in the original and attrition-milled powders.

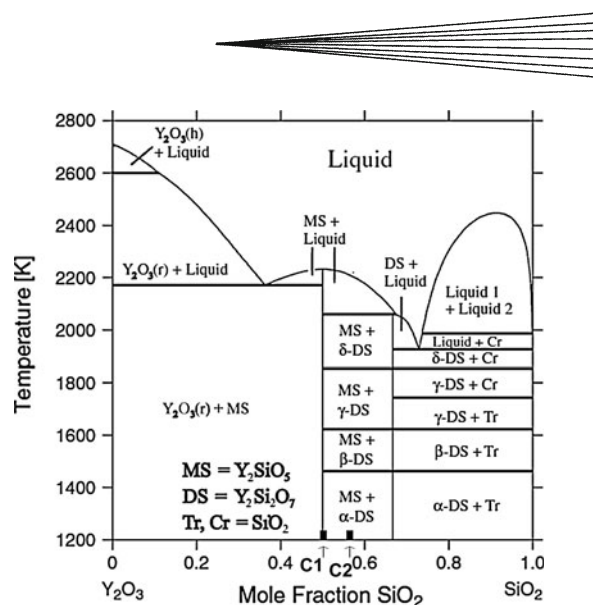


**Fig. 1** Calculated Y<sub>2</sub>O<sub>3</sub>-SiO<sub>2</sub> system (Ref 22) with the location of C1 and C2 formulated compositions

The slurries were spray-dried with a rotary atomizer system (Mobile Minor Spray Dryer, basic model, Niro Atomizer, Søborg, Denmark) in a co-current flow. The spray dryer inlet temperature ranged from 300 to 350 °C and that at exit from 100 to 150 °C. The slurry was fed at 65 mL/min and 3 × 10<sup>5</sup> Pa of air pressure. A part of the spray dried C1 batch was heat treated at 1600 °C during 3 h (labeled as C1\*) to ensure a complete reaction between the components (Ref 13).

Flame spheroidization (FS) was done by thermal spraying the C1, C1\*, and C2 feedstock with an oxygen-acetylene gun (model CastoDyn DS 8000, Eutectic Castolin, Madrid, Spain) into a water-filled metal container situated at the stand-off distance of 15 cm, in the same way as described in previous work (Ref 23). Residual water was evaporated by heating the beads at 120 °C.

Differential thermal analysis (DTA) of the FS beads were performed with a simultaneous thermal analyzer (Netzch, model 409, Germany), at a heating rate of 10 °C/min, using an alumina standard.

### 2.2 Sample Preparation

Coatings of C2 composition were deposited on SiC coupons (Hexoloy SA, Saint-Gobain, Worcester, MA, USA) previously coated with a layer of Si (Amperit 170, Germany) that was used as a bond coat. The torch input power was 28 kW, the acetylene/oxygen volumetric flow ratio was that of the stoichiometric mixture and the oxygen and acetylene pressures were 4 × 10<sup>5</sup> and 7 × 10<sup>4</sup> Pa, respectively. The stand-off distance was the same employed for FS (15 cm).

Disc-shaped specimens of 20 mm in diameter and 3 mm in thickness were obtained from beads of C2 composition by SPS (Dr Sinter 510CE, SPS Syntex Inc., Japan) at 950 °C, for 10 min, applying 80 MPa of uniaxial pressure and vacuum atmosphere (~6 Pa). Heating and cooling rates were 100 °C/min. The apparent density, measured by the Archimedes' method, was 3.97 g/cm<sup>3</sup>,

which is about 89% of the fully dense  $Y_2SiO_5$  material ( $4.44 \text{ g/cm}^3$ ). Some of the SPS samples were exposed at short high temperature treatments (SPS-HT)— $1600 \text{ }^\circ\text{C}$  during 3 h—for fully crystallization (Ref 13). The density of these samples did not vary appreciably after this treatment.

Detached coatings and SPS samples were subjected to low temperature isothermal treatment in air (LT) and under water vapor conditions (LT- $H_2O$ ) for 12 h, in a box furnace with  $Al_2O_3$  fiber insulation and  $MoSi_2$  heating elements. The temperature of  $1350 \text{ }^\circ\text{C}$  was selected as example of basic condition demanded for environmental barrier coatings (Ref 6, 24). The samples were placed inside of a cylindrical alumina crucible and covered with a lid. The crucible was connected via alumina tubes to a water evaporator, creating a water vapor flux of approximately  $4 \text{ mL/min}$ . A piece of  $SiO_2$  glass was also placed inside the alumina crucible to serve as a control sample.

### 2.3 Characterization of Powders and Samples

The microstructure of the coatings, beads, and SPS samples was viewed with a scanning electron microscope (SEM, DMS-950 Carl-Zeiss, Germany). Elemental point and area analyses for Si (K) and Y (L) were done by X-ray energy dispersive spectroscopy (EDS, Thermo Noran EF18, System Six, EEUU) on large areas of  $500 \times 500 \text{ } \mu\text{m}$  and beads (areas  $10 \times 10 \text{ } \mu\text{m}$ ). X-ray diffraction analyses (XRD, Xpert PRO, PANalytical, the Netherlands), were performed in the  $20^\circ$ – $60^\circ$   $2\theta$  range with a  $\theta/2\theta$  configuration, to track amorphization and subsequent crystallization in coatings and bulks.

Hardness ( $H$ ) was measured by Vickers micro-indentation (ZHU 2.5, Zwick GmbH & Co. KG, Germany) tests on polished cross sections of coatings (as-sprayed and aged). At least 10 measurements at a load of  $4.8 \text{ N}$  applied for 5 s were completed for each layer.

The thermal diffusivity ( $\alpha$ ) was measured on SPS samples by the laser flash method (Thermaflash 2200, Holometrix/Netzsch USA). Square-shaped samples of  $8.8 \text{ mm}$  in side and  $\sim 1 \text{ mm}$  in thickness were tested at room temperature in Ar. Thickness correction was not necessary as the surface roughness was  $< 50 \text{ } \mu\text{m}$  (Ref 25). Square surfaces were graphite coated to enhance absorption of the laser beam. Thermal conductivity ( $\kappa$ ) was calculated from specific heat ( $C_p$ ) of  $Y_2SiO_5$  (Ref 11) and density ( $\rho$ ) using the following expression:

$$\kappa = \alpha \cdot \rho \cdot C_p \quad (\text{Eq 1})$$

## 3. Results and Discussion

### 3.1 SPS Samples

Table 1 shows the results of XRF analysis for FS beads of C1, C1\*, and C2 compositions. The original C1 composition ( $0.5 \text{ SiO}_2:0.5 \text{ Y}_2\text{O}_3$ ) shifts to  $0.43 \text{ SiO}_2:0.57 \text{ Y}_2\text{O}_3$  in the beads, which supposes a  $0.07$  mol fraction reduction of  $SiO_2$ . The C1\* beads show a similar  $SiO_2$  deficient

**Table 1** XRF chemical analysis of FS beads for C1, C1\*, and C2 compositions

FS beads	$SiO_2$		$Y_2O_3$	
	wt. %	mol fract	wt. %	mol fract
C1	16.5	0.43	83.5	0.57
C1*	17.5	0.44	82.5	0.56
C2	21	0.50	79	0.50

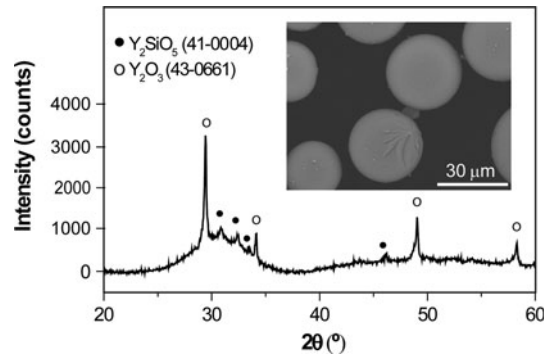


**Fig. 2** XRD pattern and SEM micrograph of as-sprayed beads of C2 composition

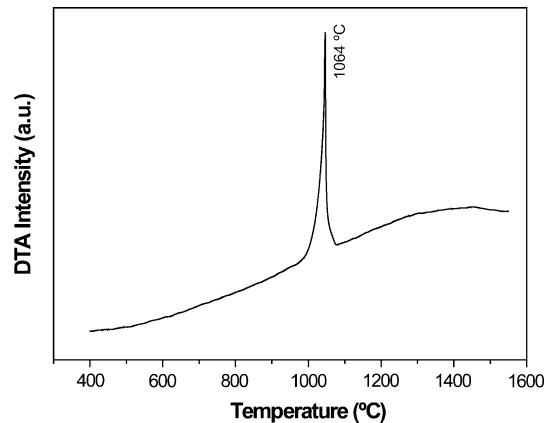


**Fig. 3** DTA curve of C2 composition FS beads

composition ( $0.44 \text{ SiO}_2:0.56 \text{ Y}_2\text{O}_3$ ). As C2 powders were formulated with an extra  $0.07$  mol fraction of  $SiO_2$ , the FS C2 beads recovered the  $0.5:0.5$  composition. These results show that by this fine-tuning of the  $SiO_2$  amount in the formulated composition, the wanted  $Y_2SiO_5$  composition is recovered. Accordingly, C2 composition was chosen for further studies, namely, the water corrosion tests and the determination of properties.

The XRD pattern of the as-sprayed FS beads of C2 composition is shown in Fig. 2. The pattern displays some sharp peaks emerging from the bulged background, the last one indicating the presence of amorphous phases. The peaks match with the face-centered cubic phase of  $Y_2O_3$  (PDF-43-0661), which is different to the starting body

centered  $Y_2O_3$  phase (PDF-41-1105). This is a strong indication that the fcc  $Y_2O_3$  detected in the beads must be recrystallized from the melt and the probably small size of these nuclei explains the smoothness of these beads, as shown in Fig. 2. Some smaller diffraction peaks that can

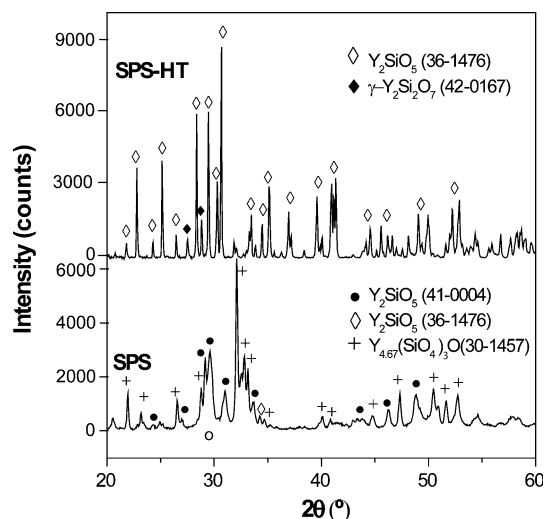
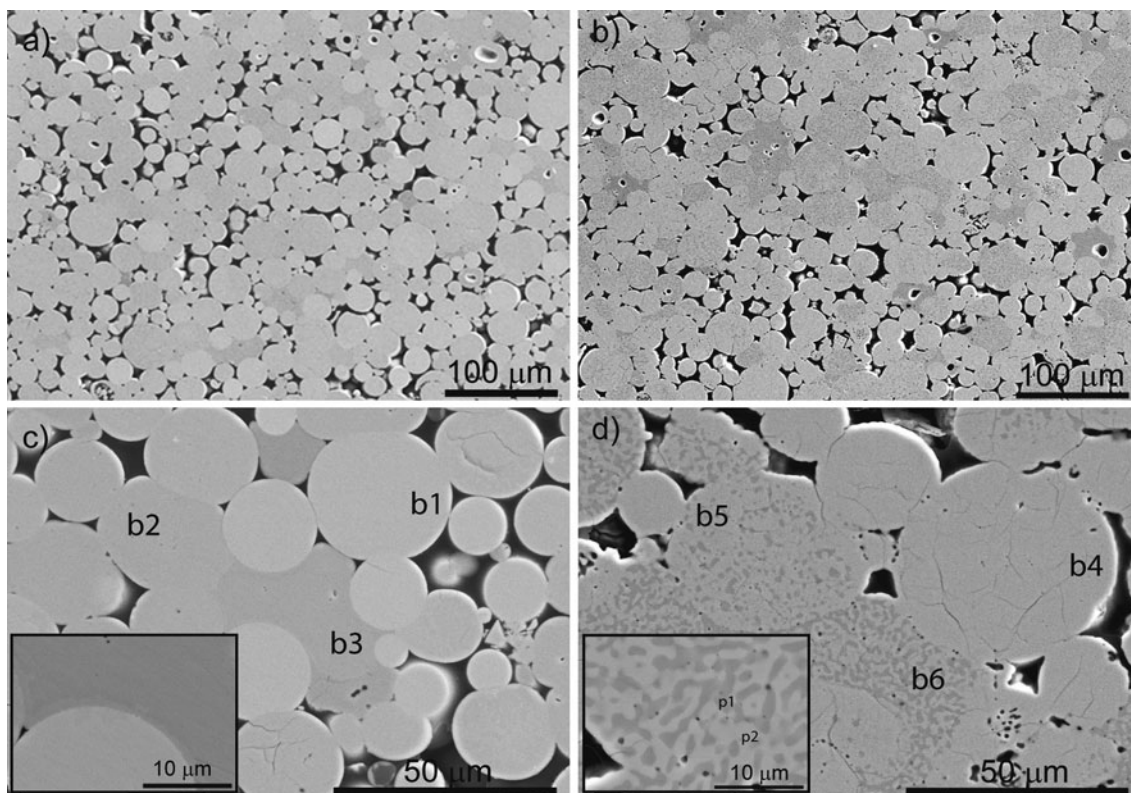


**Fig. 4** XRD patterns of the SPS samples, as-sintered and after the HT treatment (3 h at 1600 °C, SPS-HT)

be ascribed to the  $Y_2SiO_5$  phase (PDF-41-0004) are just emerging from the background of the diffraction pattern. In fact, the DTA analysis for these FS beads shows a sharp exothermic peak at 1064 °C (Fig. 3), which can be attributed to the  $Y_2SiO_5$  crystallization (Ref 9).

The temperature of 950 °C—115 °C below the crystallization temperature—was chosen for the consolidation of the FS beads in the SPS to obtain a bulk material of similar characteristics to the as-sprayed coatings.

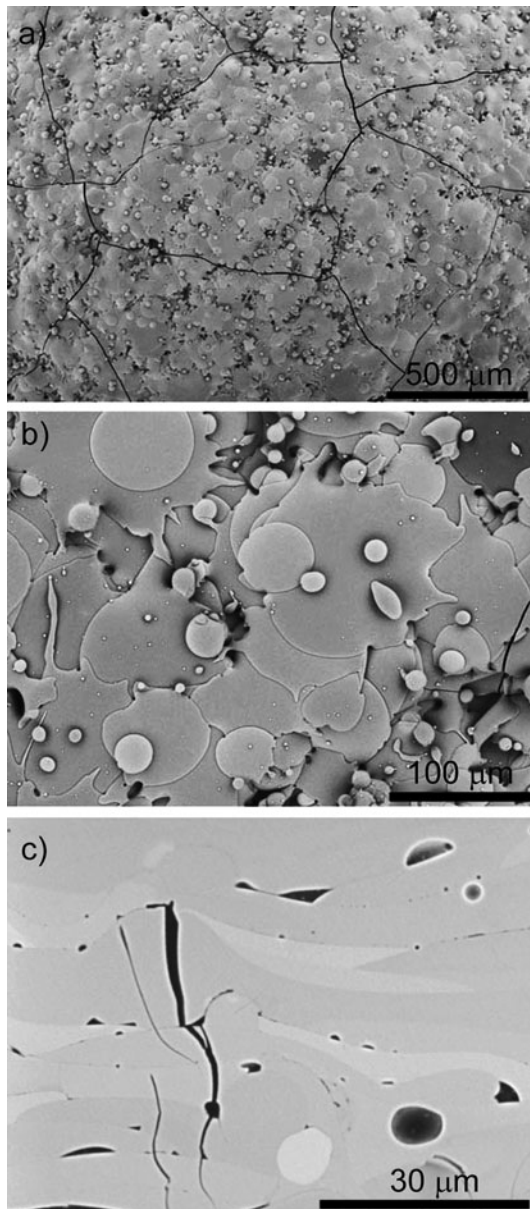
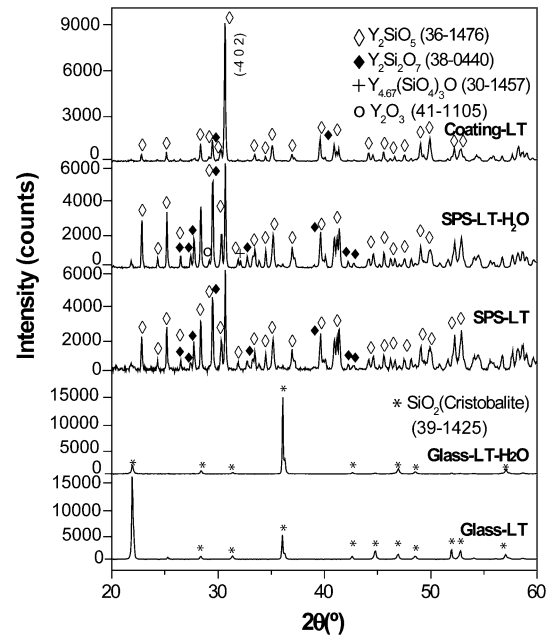
The XRD patterns for as-sintered SPS sample and for the SPS-HT, heat treated at 1600 °C, are shown in Fig. 4. The SPS sample shows the crystallization of different yttrium silicates and an amorphous background of lower intensity than that observed in the pattern of as-sprayed beads (Fig. 2). Even though SPS specimens retain some amorphous character, they certainly appear more crystalline than as-sprayed beads. The more intense peaks in the patterns correspond to a metastable O-apatite  $Y_{4.67}(SiO_4)_3O$  (PDF-30-1457), probably because of the low sintering temperature and short holding time of the SPS process. In addition, the two  $Y_2SiO_5$  monoclinic polymorphs are detected; the low temperature polymorph, like occurred in the as-sprayed beads (Fig. 2) and the high temperature  $Y_2SiO_5$  (PDF-36-1476). The presence of this high temperature polymorph is comprehensible since the transition temperature between both polymorphs is around 900 °C (Ref 11, 26), value slightly below the sintering temperature. The fast heating/cooling



**Fig. 5** SEM cross-sectional views of samples processed by SPS before (a, c) and after HT treatment (b, d). Labels indicates locations where EDS analysis were performed (Table 2)

**Table 2** EDS analysis performed on SPS and SPS-HT samples, in large areas, beads and point analysis of marked features in Fig. 5(c) and (d)

	SPS		SPS 1600		
	SiO <sub>2</sub> (mol. fract.)	Y <sub>2</sub> O <sub>3</sub> (mol. fract.)	SiO <sub>2</sub> (mol. fract.)	Y <sub>2</sub> O <sub>3</sub> (mol. fract.)	
Area 500 × 500 μm	0.50 ± 0.02	0.50 ± 0.01	Area 500 × 500 μm	0.50 ± 0.02	0.50 ± 0.01
Bead b1	0.47 ± 0.03	0.53 ± 0.01	Bead b4	0.49 ± 0.01	0.51 ± 0.01
Bead b2	0.57 ± 0.03	0.43 ± 0.01	Bead b5	0.54 ± 0.01	0.46 ± 0.01
Bead b3	0.62 ± 0.03	0.38 ± 0.01	Bead b6	0.62 ± 0.03	0.38 ± 0.01
			Pt. 1	0.62 ± 0.01	0.38 ± 0.01
			Pt. 2	0.50 ± 0.02	0.50 ± 0.01

**Fig. 6** SEM micrographs of C2 coating top views (a, b) and cross-section (c)**Fig. 7** XRD pattern of samples aged at 1350 °C during 12 h in air (LT) and under water vapor atmosphere (LT-H<sub>2</sub>O)

of SPS (presently 10 min) makes possible that both phases coexist.

The XRD pattern of the SPS-HT sample (Fig. 4) only shows the equilibrium high temperature Y<sub>2</sub>SiO<sub>5</sub> monoclinic form (PDF-36-1476), in consonance with the longer holding time at much higher temperature. This sample also presents the high temperature monoclinic  $\gamma$ -Y<sub>2</sub>Si<sub>2</sub>O<sub>7</sub> (PDF-42-0167), produced by the decomposition of metastable Y<sub>4.67</sub>(SiO<sub>4</sub>)<sub>3</sub>O phase into the equilibrium phases Y<sub>2</sub>SiO<sub>5</sub> and Y<sub>2</sub>Si<sub>2</sub>O<sub>7</sub> (Ref 27).

Figure 5 shows SEM cross-sectional views of SPS and SPS-HT samples. The SPS specimen contains well-packed FS beads that mostly preserve their spherical shape, although flattening and neck formation at the contacting points between beads are also seen (Fig. 5c). Beads with differences in grey contrast are observed—notice the color difference among beads marked b1, b2, and b3 in Fig. 5(c). All beads present smooth features, see for instance the

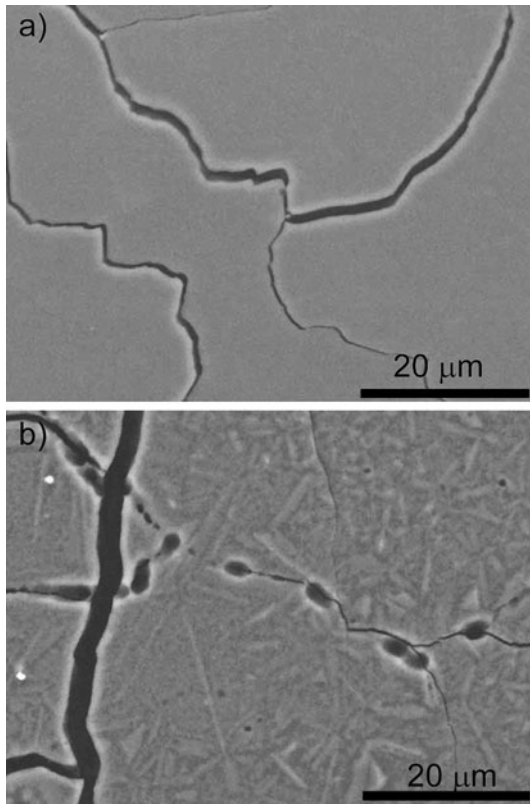
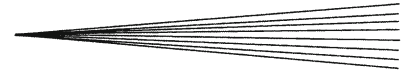


**Fig. 8** SEM micrographs of the SiO<sub>2</sub> glass samples aged at 1350 °C during 12 h in air (LT) (a) and under water vapor atmosphere (LT-H<sub>2</sub>O) (b)

high magnification image in Fig. 5(c) with no signs of crystalline nuclei, despite the XRD pattern confirms some crystallization (Fig. 4). Microstructure of the SPS-HT dramatically changes as illustrates the massive crystal nucleation (Fig. 5d). Phase separation is also perceived in the crystallized beads (b5 and b6 in Fig. 5d) and those that retain initial smoothness are fully cracked (b4 in Fig. 5d) in contrast with the as-sintered specimens where cracked beads are infrequent (Fig. 5c).

Differences in crystallization behavior and morphology between beads should be associated to compositional changes. Table 2 shows the results of the area and point EDS analysis performed on the specimens. The large area analysis reproduces the 0.5:0.5 composition, analogous result to the XRF analysis of the C2 FS beads (Table 1) and also coincident with the Y<sub>2</sub>SiO<sub>5</sub> composition, which reveals that expected composition is maintained when is averaged over a representative area—presently the EDS area analyses comprises ~3000 beads. The macroscopic homogeneity in composition is broken when beads are individually analyzed. The EDS analyses (Table 2) of representative beads marked in Fig. 5(c) and (d) show a compositional range from that of Y<sub>2</sub>SiO<sub>5</sub> (beads b1, b4 in Fig. 5c, d) to SiO<sub>2</sub> enriched composition 0.62 SiO<sub>2</sub>:0.38 Y<sub>2</sub>O<sub>3</sub> (in beads b3, b6), passing by SiO<sub>2</sub>:Y<sub>2</sub>O<sub>3</sub> proportions close to the formulated C2 powder (beads b2, b5).

The point analyses done in the two phases of the crystallized beads (p1 and p2 in the insert of Fig. 5d) reveal a

composition of Y<sub>2</sub>SiO<sub>5</sub> for the white phase, whereas the darker phase corresponds with Y<sub>2</sub>Si<sub>2</sub>O<sub>7</sub> composition. Both phases were also identified in the XRD patterns (Fig. 4).

Therefore, the idea of correcting the initial composition of the powders mixture to account for the volatilization of SiO<sub>2</sub> during thermal spraying is justified on the overall specimen. Nevertheless, local variations in composition from bead to bead are observed, attributable to differences in thermal history of the powders within the flame and during their flight towards the substrate, more than to inhomogeneities in the feedstock composition. It can be argued that this effect may be reduced using a pre-reacted mixture, but even in that case (i.e., composition C1\*), certain SiO<sub>2</sub> volatilization (0.06 mol fraction) occurs—in fact, same effect was reported for plasma-sprayed mullite coatings produced from reacted mullite (Ref 16, 19).

### 3.2 As-sprayed Coatings

The XRD pattern recorded for the as-sprayed coatings is identical to that of FS beads, as expected, because the thermal history of coatings and beads is very similar. Furthermore, in a previous study using the same rationale, the comparable crystallization scheme for flame-sprayed mullite coatings and beads with temperature was verified (Ref 28).

Figure 6 shows different views of the as-deposited coatings. The top view (Fig. 6a) reveals a network of evenly spaced cracks and the high magnification view (Fig. 6b) shows melted and flattened splats. The flat structure of the splats implies well bonded and dense coatings, as can be seen in the cross section image (Fig. 6c). In this figure, areas of different contrast are observed, as occurred for sintered SPS materials (Fig. 5a), revealing composition variations among the droplets as has also been reported in different silicate coatings processed by plasma spraying (Ref 16, 19). The vertical cracks (Fig. 6c) are linked to the crack network observed on top surface (Fig. 6a).

### 3.3 Long Temperature Treatments

Figure 7 shows the XRD patterns for the aged samples: heat treated at 1350 °C in air (LT) and under water vapor rich conditions (LT-H<sub>2</sub>O), jointly with patterns for the reference silica glass samples. Both silica samples present a diffraction pattern of cristobalite (PDF-39-1425) but that of LT-H<sub>2</sub>O glass shows variation in the intensity of peaks as compared to the corresponding XRD standard pattern, which may be produced by a preferred growing direction of the crystals. Cristobalite commonly crystallizes when silica glass is heated in either dry air or wet atmosphere (Ref 29-32), but the presence of water vapor enhances crystallization rate (Ref 29, 30) as it is also seen in the present study. It should be pointed out that some authors claim that presence of foreign impurities in the furnace atmosphere—associated to the alumina of the tubular furnaces or the parts commonly employed in the water corrosion experiments—also accounts for this enhancement (Ref 30-32). Consequently, the possible effect of

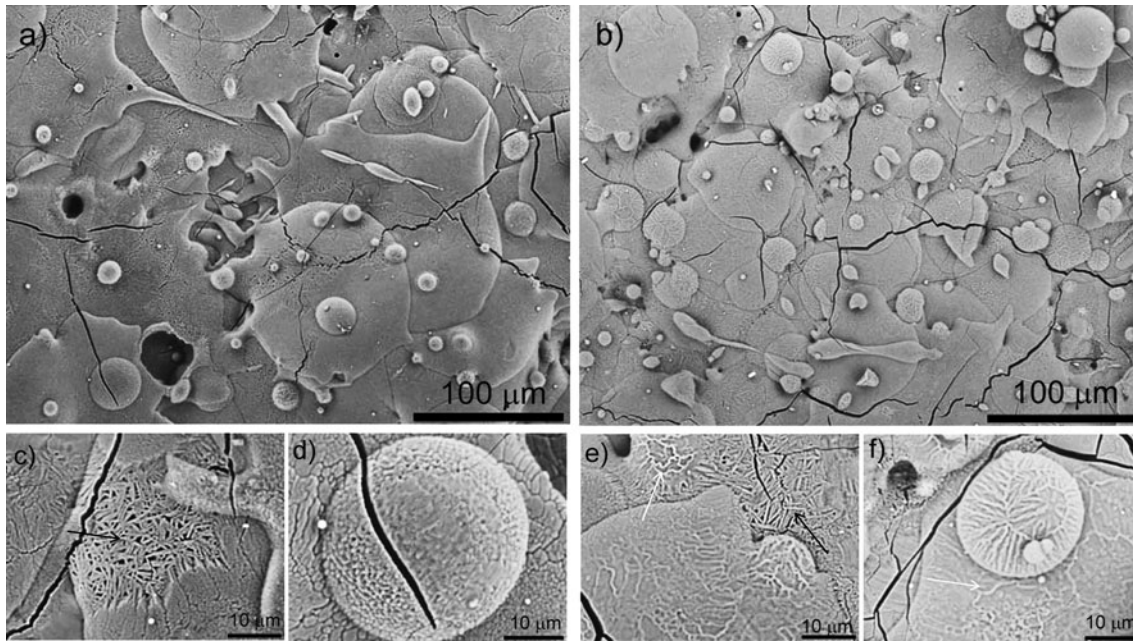


**Fig. 9** SEM micrographs of coatings top surface after thermal aging (LT) at 1350 °C for 12 h in air (a, c, d) and under water vapor atmosphere (LT-H<sub>2</sub>O) (b, e, f). Black arrows point acicular grains and white arrows show an example of ridge type structures

impurities volatilized from the alumina crucible cannot be disregarded on present tests.

The straight visual inspection of the aged SiO<sub>2</sub> glass reveals an opal appearance and shows a cracked scale (Fig. 8) that easily spalls, exposing a transparent core. This cracked layer can be definitely associated to the cristobalite detected in the XRD patterns (Fig. 7). The main microstructural difference between the air and water vapor aged samples is the presence of some small voids and needle like crystals in the LT-H<sub>2</sub>O glass sample (Fig. 8b), possibly revealed by the surface volatilization of SiO<sub>2</sub>.

The XRD patterns of the SPS samples aged in both conditions (Fig. 7) exhibit the high temperature monoclinic Y<sub>2</sub>SiO<sub>5</sub> as main crystalline phase, as occurred in the SPS sample treated at 1600 °C (SPS-HT) (Fig. 4). The next phase in intensity in the aged specimens is the monoclinic β-Y<sub>2</sub>Si<sub>2</sub>O<sub>7</sub> (PDF-38-0440) named Keiviite, phase stable at the temperature used in the LT test (1350 °C) (Ref 33). In addition, small peaks associated to the metastable Y<sub>4.67</sub>(SiO<sub>4</sub>)<sub>3</sub>O (PDF-30-1457) and Y<sub>2</sub>O<sub>3</sub> (PDF-41-1105) are detected in SPS-LT-H<sub>2</sub>O sample (Fig. 7). This could indicate that the water vapor rich atmosphere during the heat treatment indirectly favors the formation of phases with lower SiO<sub>2</sub> content than the Y<sub>2</sub>Si<sub>2</sub>O<sub>7</sub>, owing to the incipient decomposition of this phase by the SiO<sub>2</sub> volatilization.

Figure 7 also shows the XRD pattern of the air aged coating (Coating-LT), where the crystalline phases match with those found in the SPS-LT sample. The only difference is the higher intensity of the (-4 0 2) diffraction peak of Y<sub>2</sub>SiO<sub>5</sub> probably due to the layered nature of flame-sprayed coatings. This similitude in the XRD results for coatings and SPS beads again validates the use of SPS

specimens, more easy to handle and test, as a coating substitute.

In Fig. 9 different views of the top surface of the aged coatings in both dry (Fig. 9a) and water vapor conditions (Fig. 9b) are displayed; an increase in the number of cracks when compared with the as-sprayed coatings is perceived (Fig. 3b). The cracking intensification could be associated to the transformation of Y<sub>2</sub>SiO<sub>5</sub> from the low to high temperature polymorph detected in both coatings (Fig. 7), and also to its anisotropic thermal expansion coefficient with values of 0.6 and 11.7 × 10<sup>-6</sup> °C<sup>-1</sup> for *a* and *c* single crystal axes, respectively (Ref 34). Furthermore, the presence of Y<sub>2</sub>Si<sub>2</sub>O<sub>7</sub> with a thermal expansion coefficient of 4.6 × 10<sup>-6</sup> °C<sup>-1</sup> (Ref 13) almost a half of the 8.36 × 10<sup>-6</sup> °C<sup>-1</sup> reported for a single-phase polycrystalline Y<sub>2</sub>SiO<sub>5</sub> bulk material (Ref 11, 27) may aid to rise thermal stresses.

The only distinct microstructural feature in the coatings aged in H<sub>2</sub>O vapor atmosphere is the presence of ridges on the surface of a great number of splats (white arrows in Fig. 9e, f), which are also observed at the free surface of cross sectioned LT-H<sub>2</sub>O coatings (black arrow Fig. 10b) whereas in the LT coating a smoother top surface is perceived (Fig. 10a). The cross section views reveal that crystallization and the crack formation occur through the entire coating as well (Fig. 10).

The surface/volume ratio is very limited for coatings as compared to the SPS specimens that have spherical topography at the microscale and are partially porous (11 vol.%) as well, therefore the surface exposed to the furnace atmosphere is comparatively larger in the later. The exposed surface in SPS-LT materials (Fig. 11a) evidences the formation of cracks on the beads surface and a granular

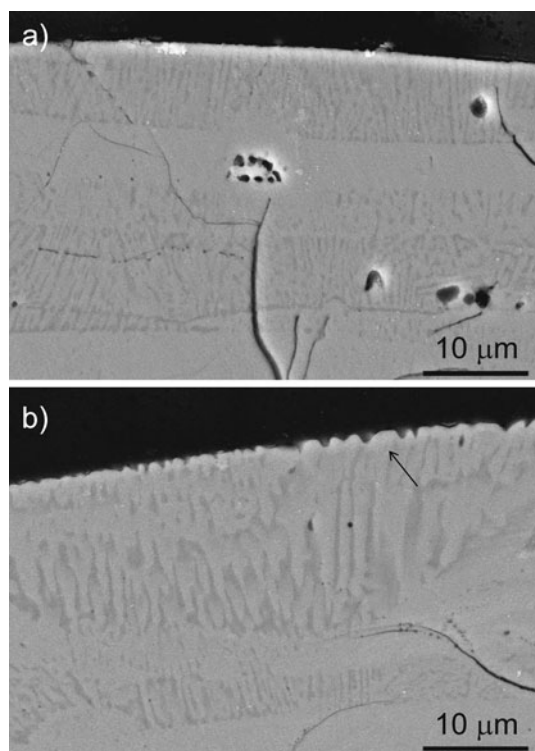


**Fig. 10** SEM micrographs of polished cross sections of the coatings after thermal aging at 1350 °C for 12 h in air (LT) (a) and under water vapor flux (LT-H<sub>2</sub>O) (b). Black arrow points the roughed surface of the LT-H<sub>2</sub>O coating

microstructure (inset in Fig. 11a). Conversely, the SPS-LT-H<sub>2</sub>O (Fig. 11b) presents the particular ridged structure on the surface of some beads (inset in Fig. 11b) also detected at the top surface of the LT-H<sub>2</sub>O coating (Fig. 9e, f). The EDS point analysis of those crests gave a composition of  $0.47 \pm 0.03 \text{ SiO}_2:0.53 \pm 0.01 \text{ Y}_2\text{O}_3$ , close to the  $\text{Y}_2\text{SiO}_5$  composition, which reasonable suggests that ridges may be produced by the selective volatilization the  $\text{SiO}_2$  from the less stable  $\text{Y}_2\text{Si}_2\text{O}_7$  phase under water vapor conditions (Ref 35) leaving the more stable  $\text{Y}_2\text{SiO}_5$  phase. Therefore, these results confirm the suitability of thermal sprayed  $\text{Y}_2\text{SiO}_5$  coatings for working in conditions similar to those developed in gas turbines, where high temperatures and water vapor atmospheres are present.

### 3.4 Properties of Processed Samples

Table 3 indicates that hardness of aged coatings (~4-5 GPa) is slightly lower than the published value for a dense  $\text{Y}_2\text{SiO}_5$  material (5.50 GPa) under similar load testing conditions (Ref 12). Surprisingly, the as sprayed coating shows a relatively higher value of hardness (6 GPa), but with more experimental scattering ( $\pm 1.5$  GPa), maybe due to the coexistence of amorphous and crystalline zones.

In Table 3 the values of thermal conductivity are reflected  $-C_p$  of  $\text{Y}_2\text{SiO}_5$  120 J/mol·K (Ref 11) was used for calculation as it matches the average composition of

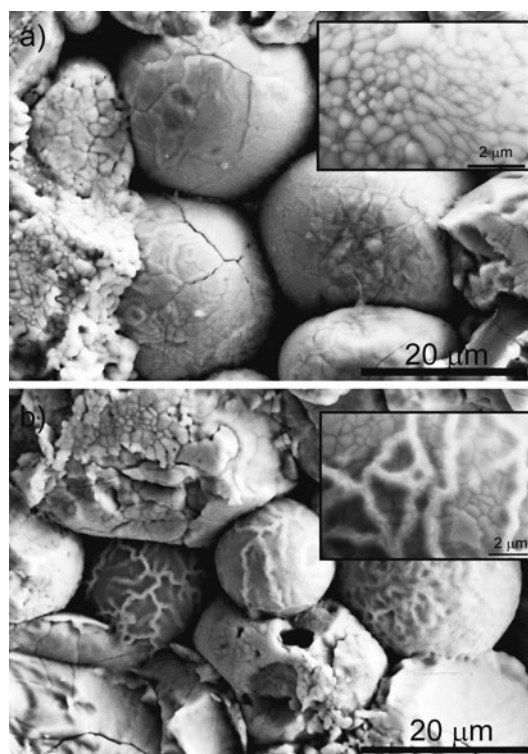


**Fig. 11** SEM micrograph of the SPS samples aged in air (LT) (a) and in water vapor atmosphere (LT-H<sub>2</sub>O) (b). The insets show higher magnification views of the beads surface

**Table 3** Hardness and room temperature thermal conductivity of coatings and SPS materials. Corresponding data after treatments LT and LT-H<sub>2</sub>O (see text) are also included

Coatings	Hardness, GPa	SPS Sample	Thermal conductivity, W/K·m
As sprayed	$6.0 \pm 1.5$	As-sinter	$0.8 \pm 0.1$
LT	$5.0 \pm 0.3$	LT	$2.1 \pm 0.1$
LT-H <sub>2</sub> O	$4.2 \pm 0.1$	LT-H <sub>2</sub> O	$2.3 \pm 0.1$

the samples. The density of the samples did not vary appreciably after aging tests and the value of  $3.97 \text{ g/cm}^3$  was used in Eq 1. An important increment in thermal conductivity is observed after aging tests of almost three times the conductivity of the initial SPS sample. The values for aged samples are both very similar, indicating that the water vapor corrosion has no effect on this property, as it is mainly a surface phenomenon. The thermal conductivity values (2.1 and 2.3 W/K·m) of the crystallized samples are higher than those reported for bulk  $\text{Y}_2\text{SiO}_5$  (1.9 W/K·m, data extrapolated to room temperature from Ref 11), which can be explained by presence of  $\text{Y}_2\text{Si}_2\text{O}_7$  in the samples, with a thermal conductivity of 4.9 W/m·K (extrapolated to room temperature from data reported in Ref 36).

Therefore, the higher conductivity obtained in aged SPS specimens compared to the as-sinter specimen is produced



by the extensive crystallization and does not seem much affected by the crack network. Similar effect can be expected to occur in the aged coatings.

## 4. Summary

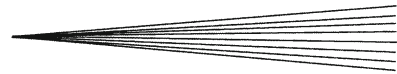
It is challenging to achieve stoichiometric and homogeneous  $Y_2SiO_5$  coatings by thermal spraying methods as the chemical composition of the coating varies from point to point. As-sprayed coatings are predominantly amorphous, which induces cracking upon heating at high temperatures, thus affecting the mechanical integrity of the coatings. The use of SPS to consolidate flame spheroidized beads is valuable for predicting the microstructure and properties of  $Y_2SiO_5$  coatings as they are convenient bulk substitutes. Although volatilization of  $SiO_2$  species from the accompanying  $Y_2Si_2O_7$  phase was detected after water vapor tests, the formation of a ridged microstructure in the surface of coatings and SPS beads with  $Y_2SiO_5$  composition validates the performance of this phase for its use as environmental barrier coating in environments typical of combustion conditions. The temperature of the aging increases three times the thermal conductivity of SPS specimens owing to the crystallization effects but does not change appreciably the coating hardness.

## Acknowledgments

This work was supported by the Spanish Ministry of Economy and Competitiveness (MINECO) under project number MAT2009-09600. Dr. E. Garcia acknowledges the financial support of the Ramon y Cajal Program of the MINECO

## References

- H. Kaya, The Application of Ceramic-Matrix Composites to the Automotive Ceramic Gas Turbine, *Compos. Sci. Technol.*, 1999, **59**, p 861-872
- H. Ohnabe, S. Masaki, M. Onozuka, K. Miyahara, and T. Sasa, Potential Application of Ceramic Matrix Composites to Aero-engine Components, *Composites: Part A*, 1999, **30**, p 489-496
- M.E. Westwood, J.D. Webster, R.J. Day, F.H. Hayes, and R. Taylor, Oxidation Protection for Carbon Fiber Composites, *J. Mater. Sci.*, 1996, **31**, p 1389-1397
- E.J. Opila and R. Hann, Paraline Oxidation of CVD SiC in Water Vapor, *J. Am. Ceram. Soc.*, 1997, **80**, p 197-205
- J.L. Smialek, R.C. Robinson, E.J. Opila, D.S. Fox, and N.S. Jacobson, SiC and  $Si_3N_4$  Scale Volatility Under Combustor Conditions, *Adv. Compos. Mater.*, 1999, **8**, p 33-45
- H.E. Eaton, G.D. Linsey, E.Y. Sun, N. Miriyala, A. Fahme, and M. van Roode, Ceramic Stationary Gas Turbine Program—Combustor Liner Development Summary, ASME Paper 2001-GT-512, presented at the International Gas Turbine and Aeroengine Congress and Exposition, New Orleans, LA, USA, June 2001
- K.N. Lee, D.S. Fox, and N.P. Bansal, Rare Earth Silicate Environmental Barrier Coatings for SiC/SiC Composites and  $Si_3N_4$  Ceramics, *J. Am. Ceram. Soc.*, 2005, **25**, p 1705-1715
- Y. Ogura, M. Kondo, and T. Morimoto,  $Y_2SiO_5$  as Oxidation-Resistant Coating for C/C Composites, *Proceedings of the Tenth International Conference on Composite Materials*, Vol. IV (Whistler British Columbia, Canada, Aug 14-18, 1995), A. Poursartip and K. Street, Ed., Woodhead Publishing, Oxford, 1995, p 767-774
- D. Boyer and B. Derby, Yttrium Silicate Powders Produced by the Sol-Gel Method, Structural and Thermal Characterization, *J. Am. Ceram. Soc.*, 2003, **86**, p 1595-1597
- Z.Q. Sun, Y.C. Zhou, and M.S. Li, Effect of  $LiYO_2$  Additive on Synthesis and Pressureless Sintering of  $Y_2SiO_5$ , *J. Mater. Res.*, 2008, **23**, p 732-736
- Z.Q. Sun, Y.C. Zhou, and M.S. Li, Thermal Properties of Single-Phase  $Y_2SiO_5$ , *J. Eur. Ceram. Soc.*, 2009, **29**, p 551-557
- Z.Q. Sun, J.Y. Wang, M.S. Li, and Y.C. Zhou, Mechanical Properties and Damage Tolerance of  $Y_2SiO_5$ , *J. Eur. Ceram. Soc.*, 2008, **28**, p 2895-2901
- M. Aparicio and A. Durán, Yttrium Silicate Coatings for Oxidation Protection of Carbon-Silicon Carbide Composites, *J. Am. Ceram. Soc.*, 2000, **83**, p 1351-1355
- Chr Argirusis, T. Damjanovic, and G. Borchardt, Yttrium Silicate Coating System for Oxidation Protection of C/C-Si-SiC Composites: Electrophoretic Deposition and Oxygen Self-Diffusion Measurements, *J. Eur. Ceram. Soc.*, 2007, **27**, p 1303-1306
- X. Zheng, Y. Du, J. Xiao, Y. Lu, and C. Liang, Celsius/Yttrium Silicate Protective Coating Prepared by Microwave Sintering for C/SiC Composites Against Oxidation, *Mat. Sci. Eng. A*, 2009, **505**, p 187-190
- E. Garcia, J. Mesquita-Guimarães, P. Miranzo, M.I. Osendi, C.V. Cojocar, Y. Wang, C. Moreau, and R.S. Lima, Phase Composition and Microstructural Responses of Graded Mullite/YSZ Coatings Under Water Vapor Environments, *J. Therm. Spray Technol.*, 2011, **20**, p 83-91
- Y. An, G. Liu, X. Zhao, J. Chen, H. Zhou, and G. Hou, Preparation and Microstructure Characterization of Mullite Coatings Made of Mullitized Natural Andalusite Powders, *J. Therm. Spray Technol.*, 2011, **20**, p 485-489
- J.F. Huang, H.J. Li, X.R. Zeng, and K.Z. Li, Yttrium Silicate Oxidation Protective Coating for SiC Coated Carbon/Carbon Composites, *Ceram. Int.*, 2006, **32**, p 417-421
- H.J. Seifert, S. Wagner, O. Fabrichnaya, H.L. Lukas, Fritz Aldinger, T. Ullmann, M. Schmucker, and H. Schneider, Yttrium Silicate Coatings on Chemical Vapor Deposition SiC-Precoated C/C-SiC: Thermodynamic Assessment and High-Temperature Investigation, *J. Am. Ceram. Soc.*, 2005, **88**, p 424-430
- E. Garcia, P. Miranzo, R. Soltani, and T.W. Coyle, Microstructure and Thermal Behavior of Thermal Barrier Coatings, *J. Therm. Spray Technol.*, 2008, **14**, p 478-485
- E. Garcia, M.I. Osendi, and P. Miranzo, Porous Mullite Templated from Hard Mullite Beads, *J. Eur. Ceram. Soc.*, 2011, **31**, p 1397-1403
- O. Fabrichnaya, H.J. Seifert, R. Weiland, T. Ludwig, F. Aldinger, and A. Navrotsky, Phase Equilibria and Thermodynamics in the  $Y_2O_3-Al_2O_3-SiO_2$  System, *Z. Metallkd.*, 2001, **92**, p 1083-1097
- E. Garcia, J. Mesquita-Guimarães, P. Miranzo, M.I. Osendi, C.V. Cojocar, Y. Wang, C. Moreau, and R.S. Lima, Mullite and Mullite/ZrO<sub>2</sub>-7wt.% Y<sub>2</sub>O<sub>3</sub> Powders for Thermal Spraying of Environmental Barrier Coatings, *J. Therm. Spray Technol.*, 2010, **19**, p 286-293
- J. Mesquita-Guimarães, E. Garcia, P. Miranzo, M.I. Osendi, C.V. Cojocar, and R.S. Lima, Mullite-YSZ Multilayered Environmental Barrier Coatings Tested in Cycling Conditions Under Water Vapor Atmosphere, *Surf. Coat. Technol.*, 2012, **209**, p 103-109
- E. Garcia, M.I. Osendi, and P. Miranzo, Thermal Diffusivity of Porous Cordierite Ceramic Burners, *J. Appl. Phys.*, 2002, **92**, p 2346-2349
- J.W. Nowok, J.P. Kay, and R.J. Kulas, Thermal Expansion and High Temperature Phase Transformation of the Yttrium Silicate  $Y_2SiO_5$ , *J. Mater. Res.*, 2001, **16**, p 2251-2255
- J. Parmentier, K. Liddell, D.P. Thompson, H. Lemerrier, N. Schneider, S. Hampshire, P.R. Bodart, and R.K. Harris, Influence of Iron on the Synthesis and Stability of Yttrium Silicate Apatite, *Solid State Sci.*, 2001, **3**, p 495-502



28. E. Garcia, J. Mesquita-Guimarães, P. Miranzo, and M.I. Osendi, Crystallization Studies in Mullite and Mullite-YSZ Beads, *J. Eur. Ceram. Soc.*, 2010, **30**, p 2003-2008
29. L.U. Obuji, Development of Oxide Scale Microstructure on Single-Crystal SiC, *J. Mater. Sci.*, 1981, **16**, p 2753-2759
30. M. Maeda, K. Nakamura, and T. Ohkubo, Oxidation of Silicon Carbide in a Wet Atmosphere, *J. Mater. Sci.*, 1988, **23**, p 3933-3938
31. E. Opila, Influence of Alumina Reaction Tube Impurities on the Oxidation of Chemically-Vapor-Deposited Silicon Carbide, *J. Am. Ceram. Soc.*, 1995, **78**, p 1107-1110
32. E. Opila, Variation of the Oxidation Rate of Silicon Carbide with Water Vapor Pressure, *J. Am. Ceram. Soc.*, 1999, **82**, p 625-636
33. J. Ito and H. Johnson, Synthesis and Study of Yttrialite, *Am. Miner.*, 1968, **53**, p 1940-1952
34. H.M. O'Bryan, P.K. Gallagher, and G.W. Berkstresser, Thermal Expansion of  $Y_2SiO_5$  Single Crystals, *J. Am. Ceram. Soc.*, 1988, **71**, p 42-43
35. H. Klemm, Silicon Nitride for High-Temperature Applications, *J. Am. Ceram. Soc.*, 2010, **93**, p 1501-1522
36. Z.Q. Sun, Y.C. Zhou, J.Y. Wang, and M.S. Li, Thermal Properties and Thermal Shock Resistance of  $\gamma$ - $Y_2Si_2O_7$ , *J. Am. Ceram. Soc.*, 2008, **91**, p 2623-2629